

Searches for new physics in $t\bar{t}$ pair production at the Large Hadron Collider

Candidate

Antonella Succurro

Supervised by

Dr. Aurelio Juste Rozas

Institució Catalana de Recerca i Estudis Avancat

Institut de Física d'Altes Energies

Professore: Lei ha una qualche ambizione?

Nicola: Ma... Non...

Professore: E Allora vada via... Se ne vada dall'Italia. Lasci l'Italia finché è in tempo.
Cosa vuole fare, il chirurgo?

Nicola: Non lo so, non ho ancora deciso...

Professore: Qualsiasi cosa decida, vada a studiare a Londra, a Parigi... Vada in
America, se ha le possibilità, ma lasci questo Paese. L'Italia è un Paese da
distruggere: un posto bello e inutile, destinato a morire.

Nicola: Cioè, secondo lei tra poco ci sarà un'apocalisse?

Professore: E magari ci fosse, almeno saremmo tutti costretti a ricostruire... Invece
qui rimane tutto immobile, uguale, in mano ai dinosauri. Dia retta, vada via...

da La meglio Gioventù di M.T. Giordana (2003)

⁴ Introduccion

⁵

Contents

8	Introduction	ix
9	1 Going beyond the Standard Model	1
10	1.1 Building the Standard Model	1
11	1.2 New Physics Models predicting vector-like quarks	1
12	2 The ATLAS experiment at the Large Hadron Collider	3
13	2.1 The ATLAS detector	6
14	2.1.1 Coordinate system	7
15	2.1.2 Magnets	9
16	2.1.3 Inner detector	9
17	2.1.4 Calorimeters	11
18	2.1.5 Muon spectrometer	14
19	2.1.6 Trigger system	16
20	2.2 Object reconstruction	17
21	2.2.1 Electrons	17
22	2.2.2 Muons	18
23	2.2.3 Jets	19
24	2.2.4 Missing transverse energy	19
25	3 Monte Carlo simulation	21
26	3.1 Parton shower	21
27	3.2 Hadronization	21
28	3.3 Underlying-event	21
29	3.4 Generators	21
30	4 Searches for vector-like top partner pairs in the single lepton channel	23
31	4.1 Common event preselection and orthogonality	24
32	4.2 Datasets	24

33	4.2.1	Data sample	24
34	4.2.2	Monte Carlo simulated samples	24
35	4.2.3	Multi-jet background	24
36	4.3	Search for $T\bar{T}$ pairs decaying to $Wb + X$	24
37	4.3.1	Boosted W reconstruction	24
38	4.3.2	Control regions	24
39	4.3.3	Event selection	24
40	4.3.4	24
41	4.3.5	24
42	4.3.6	Systematics	24
43	4.4	Preliminary search for $T\bar{T}$ pairs decaying to $Ht + X$	24
44	4.4.1	Control regions	24
45	4.4.2	Event selection	24
46	4.4.3	24
47	4.4.4	24
48	4.4.5	Systematics	24
49	5	Statistical treatment and Results	25
50	5.1	The CL_s method	25
51	5.2	Results	25
52		Conclusions	27
53		A	29
54		B	31
55	C	Search for $T\bar{T} \rightarrow Wb + X$ at $\sqrt{7}$ TeV	33
56		Bibliography	35

57 **Introduction**

58

60 Going beyond the Standard Model

61

62 The Standard Model (SM) of particle physics is the most successful, beautiful and
63 precise theory describing the interactions between fundamental particles. Its validity has
64 been tested by precision measurements at the Large Electron-Positron Collider (LEP) at
65 CERN and confirmed by the observation of all the particles it predicts, including the Higgs-
66 like boson discovered at the Large Hadron Collider (LHC) in July of 2012 which up to now
67 behaves as expected from the SM.

68 What makes the SM “only” and effective theory is the fact that unstabilities appear at
69 high energy scales of the order of the Planck mass. In this Chapter we will show

70 1.1 Building the Standard Model

71 1.2 New Physics Models predicting vector-like quarks

72 [1, 2]

74 The ATLAS experiment at the Large 75 Hadron Collider

76

77 The analyses presented in this dissertation have been performed analyzing data from
78 proton-proton (p-p) collisions at the center of mass energy $\sqrt{s} = 8$ TeV recorded during the
79 year 2012 at the ATLAS experiment [3]. In the following Chapter we will briefly describe
80 the main features of the detector, located at the CERN laboratories in Geneva, Switzerland.

81 The experimental facilities are situated at Point 1 along the Large Hadron Collider
82 (LHC) [4] 27 km long ring, shown in Figure 2.1. The accelerator tunnel can reach an
83 underground depth of 175 meters and is spread between Swiss and French territory, while
84 the cave where ATLAS is allocated is about 100 meters underground in the CERN Swiss
85 site of Meyrin.

86 The LHC program was approved by CERN Council in 1994, followed by the approval of
87 the four main experiments physics programs: ATLAS [3] and CMS [5] in 1996; ALICE [6] in
88 1997; LHCb [7] in 1998. Works towards the installation of the most powerful particle accel-
89 erator of the world started when the Large Electron Positron Collider (LEP) was dismantled
90 in 2000 to give up its place in the tunnel to the LHC, which was then fully operational by
91 2008.

92 The LHC is composed of eight arcs 2.7 km long, each of which contains 154 dipole mag-
93 nets, whose function is to bend the beams along the circular trajectory, and 49 quadrupole
94 magnets, that focus the beam. These superconducting magnets operate at a temperature
95 of 1.9 K, maintained by means of liquid Helium vessels. Eight insertions are placed inbe-
96 tween the arches. Each insertion has a specific role that characterizes its design and can be
97 injection, beam dumping, beam cleaning, or “physics”, i.e. make the beams collide within
98 an experiment.

99 First proton beams were circulated on 10th September 2008 and right on the verge
100 of getting the first collisions at a center of mass energy $\sqrt{s} = 900$ GeV nine days later, an
101 electrical connection joining superconducting wires of a dipole and a quadrupole failed. This
102 caused the release of liquid Helium in the insulating vacuum, resulting in an explosion that
103 severely damaged the machine. After more than one year devoted to repair the damage

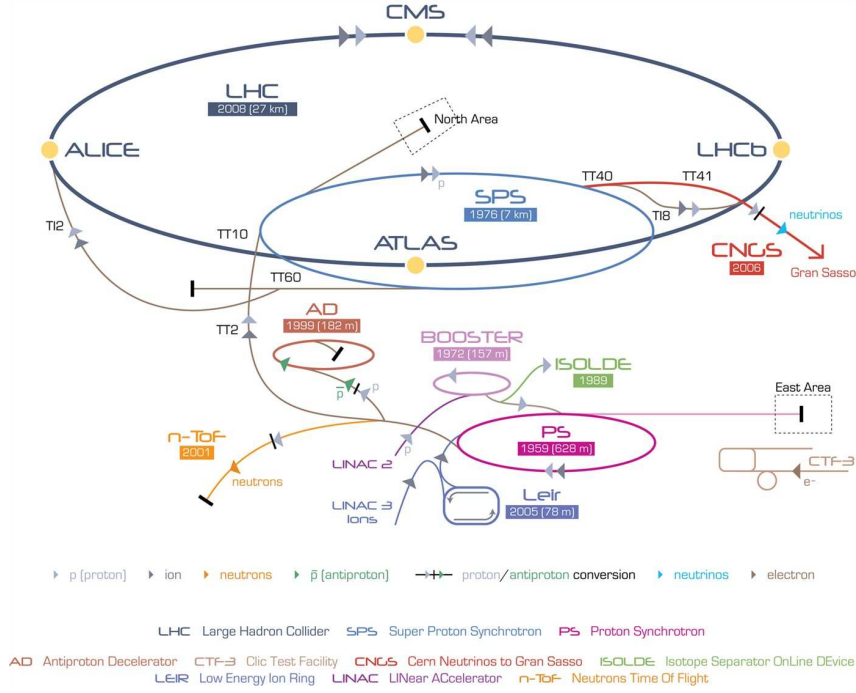


Figure 2.1: A schematic showing the accelerator complex at CERN. Protons are extracted from Hydrogen gas and injected in the first machine, the linear accelerator LINAC2 that starts the acceleration chain. When protons reach an energy of 50 MeV they are injected into the Proton Synchrotron Booster (PSB) and accelerated up to the energy of 1.4 GeV. The second circular accelerator, the Proton Synchrotron (PS) brings the energy of the protons to 25 GeV previous to injecting them into the last machine before the LHC, the Super Proton Synchrotron (SPS). Protons of 450 GeV finally enter the LHC where they are boosted to energies of up to 4 TeV. The four main LHC experiments are shown on the collider ring.

and consolidate the security, on 30th November 2009 the LHC became the world's highest energy particle accelerator¹:

Geneva, 30 November 2009. CERN's Large Hadron Collider has today become the worlds highest energy particle accelerator, having accelerated its twin beams of protons to an energy of 1.18 TeV in the early hours of the morning. This exceeds the previous world record of 0.98 TeV, which had been held by the US Fermi National Accelerator Laboratorys Tevatron collider since 2001. It marks another important milestone on the road to first physics at the LHC in 2010.

The main performance figure of merit for an accelerator is the luminosity, the instantaneous luminosity \mathcal{L} being defined as

$$\mathcal{L} \times \sigma = \frac{dN}{dt} = f \times n \frac{N_1 \times N_2}{A} \times \sigma. \quad (2.1)$$

Here dN/dt is the event rate of a certain process and σ is its cross section. This rate is directly proportional to the the frequency f , the number of bunches n and the number of particles in the two bunches N_1, N_2 , and inversely proportional to the beam cross-section A .

¹<http://press.web.cern.ch/press/PressReleases/Releases2009/PR18.09E.html>

Parameter	designed	2010	2011	2012
Beam energy (TeV/c)	7	3.5	3.5	4
Beta function β^* (m)	0.55	2.0/3.5	1.5/1.0	0.6
Max. No. bunches/beam	2808	368	1380	1380
Max. No. protons/bunch	1.15×10^{11}	1.2×10^{11}	1.45×10^{11}	1.7×10^{11}
Bunch spacing (ns)	25	150	75/50	50
Peak luminosity ($\text{cm}^{-2}\text{s}^{-1}$)	1×10^{34}	2.1×10^{32}	3.7×10^{33}	7.7×10^{33}
Emittance ε_n (μrad)	3.75	2.0	2.4	2.5

Table 2.1: Overview of some parameters for the LHC performance comparing the design values with their time evolution during the first long run operation in 2010-2013 [8].

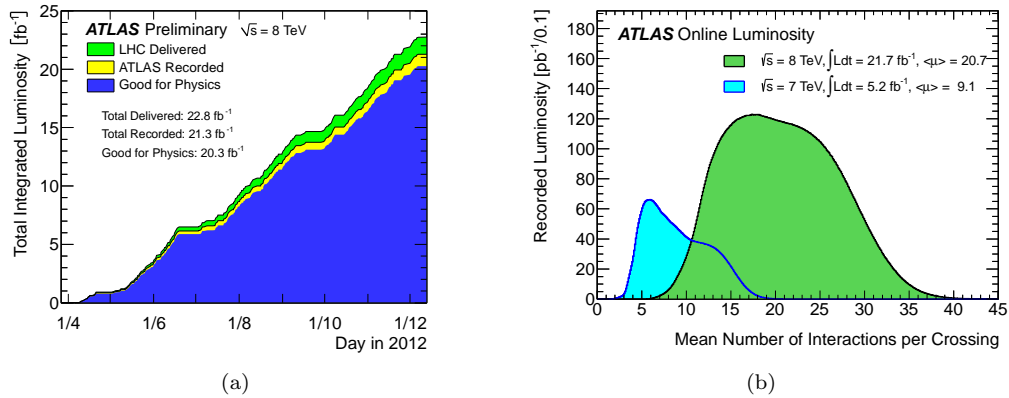


Figure 2.2: (a) Total integrated luminosity versus time delivered by the LHC to ATLAS (in green), recorded by the experiment (in yellow) and selected as “good data” for analysis (in blue) for p-p collisions at $\sqrt{s}=8 \text{ TeV}$. (b) Mean number of interactions per beam crossing during 2011 and 2012 LHC runs, where $\mu = \mathcal{L} \times \sigma_{\text{inelastic}}/f$ depends on the instantaneous luminosity \mathcal{L} , the p-p inelastic cross section $\sigma_{\text{inelastic}}$ and the revolution frequency f . [9]

Integrating over the accelerator active time (a “fill”, when stable beams are kept colliding) gives the *integrated luminosity*, relating the total number of produced events N_{tot} to the cross-section:

$$\int \mathcal{L} dt = \frac{N_{\text{tot}}}{\sigma}. \quad (2.2)$$

In 2012 LHC reached a peak luminosity of $7.7 \times 10^{33} \text{ cm}^{-2}\text{s}^{-1}$ which is more than half the design luminosity, as shown in Table 2.1 together with other parameters relevant for the accelerator performance. Over the last year of data taking before the long shutdown² ATLAS collected about 20 fb^{-1} of p-p collision data at $\sqrt{s}=8 \text{ TeV}$. Figure 2.2(a) shows the delivered luminosity from the start of stable beams until beam dump and the luminosity recorded by ATLAS during stable beam conditions, the difference with respect to the delivered luminosity being due to Data Acquisition (DAQ) inefficiencies. Of the recorded luminosity, only a part

²LHC terminated the p-p program at the end of 2012, operated proton-heavy ion collisions for two months at the beginning of 2013 and then stopped for what is called the first long shutdown. During this two-years time the accelerator and the experiments as well will undergo substantial maintenance and upgrade works, in order to be re-operated in 2015 with higher performance at a higher center of mass energy for particle collisions.

is usable for analysis, and is what is called “good data”, i.e. the data that satisfy Data Quality (DQ) requirements assessed after reprocessing.

In order to increase the luminosity LHC operates with a high number of protons per bunch as well as a high number of bunches per beam and reduces the inter-bunch latency time. This overall defines a set of challenges that physics analysis will face associated to the high luminosity. Even at the detector design stage, the high frequency of collision environment foreseen influenced the choice of radiation resistance material for the experiment sub-systems. Concerning directly the physics instead we can list the main problematics as being *underlying events* and *pile-up*

Underlying events are the product of the hadronic character of p-p hard interaction, where the main collision process is accompanied by secondary parton interactions at low transferred momentum (soft QCD) and are flavor- and color-connected to the hard scattering. They are observed as jets of particles close to the direction of the beam and are in general not separable from the event of interest. Their contribution can be studied with Monte Carlo techniques tuned with data from *minimum bias* events, as perturbative theory does not properly model low momentum QCD.

Pile-up events are distinguished between *in-time* and *out-of-time* pile-up. The first ones come from the multiple inelastic scatterings of protons in the same bunch, as if we consider a cross-section of 80 mb at the nominal luminosity of $10^{34} \text{ cm}^{-2}\text{s}^{-1}$ the number of events per second will be something like a billion. This translate, at a collision frequency of one crossing every 25 ns, to about 20 interactions per crossing that will be detected simultaneously. On the other hand, the inter-bunch time interval is so short that the electronics reading the detector might not keep up with the frequency of collisions, leading to the cumulation of events that happened in different beam crossings.

ATLAS makes use of a three-level trigger system (described in Section 2.1.6) to identify and record only the events of interest, while the pile-up issues are dealt with at the analysis reconstruction level.

2.1 The ATLAS detector

ATLAS (A Toroidal LHC ApparatuS) [3] is a general purpose experiment aimed at exploring a vast range of physics scenarios. It is characterized by a full coverage of the space around the p-p interaction point and complete containment of the particles produced in the collision. Different subsystems are layered concentrically one after the other, each of them pursuing a specific task. Right around the interaction point (IP) where the LHC makes protons collide there is the Vertex Detector, reconstructing charged particles trajectories that are bended by the first solenoid magnet surrounding the Vertex Detector. Particles going through it then encounter the two calorimeter systems, the Electromagnetic and the Hadronic one. Muons are the only particles that will pass the calorimeters material (beyond neutrinos) and a dedicated Muon Spectrometer is the last piece of detector, embedded in a huge toroidal magnet. The detector complex is presented as a schematic in Figure 2.3.

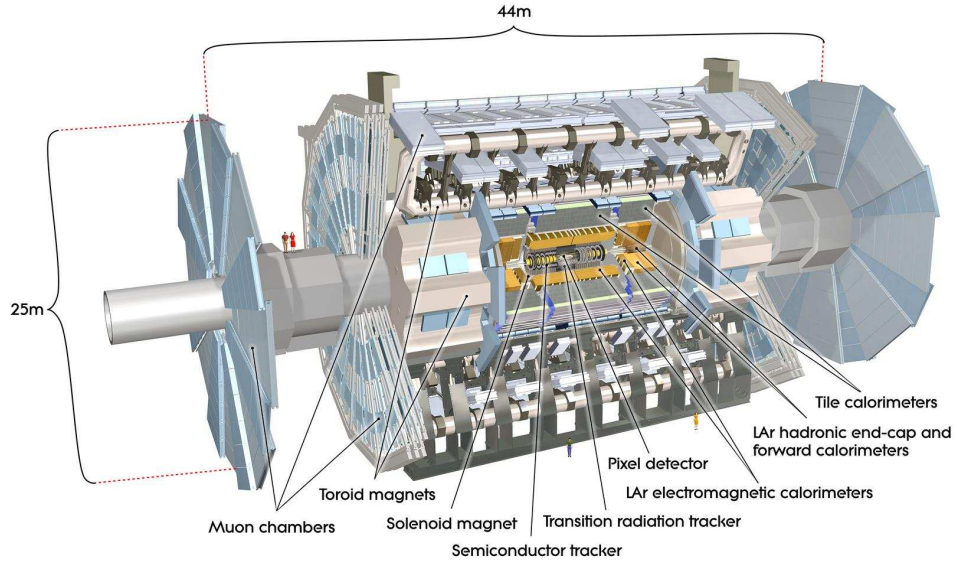


Figure 2.3: Schematic drawing of the ATLAS experiment. The detector subsystem are indicated as well as the total dimensions.

2.1.1 Coordinate system

Protons from the two circulating beams are made to collide in the center of the ATLAS detector, in the region that takes the name of Interaction Point (IP). The IP is taken as the origin of a three dimensional XYZ right-handed coordinate system. The Z axis is tangent to the trajectory of the beams while the XY plane is perpendicular to it and defines a symmetry plane for the detector, dividing it into the A and C sectors, respectively in the positive and negative Z semi-axes. Figure 2.4(a) shows a schematic of the coordinate system.

In terms of polar coordinates, the Z axis is again along the beam axis and in the transverse plane the R and ϕ coordinates are defined with ϕ ranging between $-\pi$ and $+\pi$ with respect to the X axis. In terms of spherical coordinates (see Figure 2.4(b)), the radial vector R originates from the IP, the azimuth ϕ is the same as the polar angle ϕ , and the polar angle θ is measured with respect to the Z axis and ranges between 0 and π .

Since the interaction initial energy is unknown, being dependent on the parton distribution functions for the proton energy, it is useful to define the transverse component of variables of interest³ like the energy and the momentum, being taken as the projection on the XY plane:

$$E_T = E \sin \theta, \quad p_T = p \sin \theta. \quad (2.3)$$

Another common variable used at hadron colliders to describe the polar distribution and

³These quantities transverse initial value will be, indeed, zero, as the protons are accelerated along the Z axis.

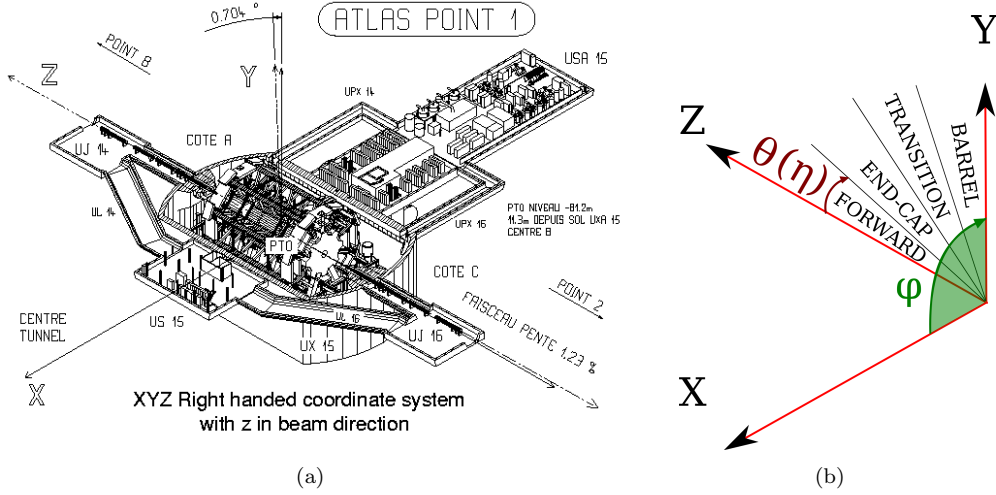


Figure 2.4: (a) Drawing of the ATLAS experiment with the cartesian coordinate system. The positive X axis points towards the center of the LHC ring. The positive Z axis points towards the anti-clockwise circulating direction of beam 2. (b) Simple schematic showing the spherical coordinates and the region definition in terms of the absolute value of the pseudorapidity η . These regions are symmetrical with respect to the transverse XY plane.

preferred to the simple polar angle θ is the pseudorapidity η :

$$\eta \equiv -\ln \left(\tan \frac{\theta}{2} \right); \quad (2.4)$$

which, for relativistic regimes, is equal to the rapidity y :

$$y \equiv \frac{1}{2} \ln \left(\frac{E + p_Z}{E - p_Z} \right); \quad (2.5)$$

and Δy and $\Delta \eta$ are Lorentz invariant. The pseudorapidity is preferred to the rapidity as it does not require knowing the particle mass but only its polar position. The distance between two particles is often referred to in terms of ΔR :

$$\Delta R = \sqrt{\Delta^2 \eta + \Delta^2 \phi}. \quad (2.6)$$

Figure 2.4(b) shows how different pseudorapidity regions are named. Particles along the Z axis have a pseudorapidity $|\eta| = \infty$, particles along the Y axis have a pseudorapidity $|\eta| = 0$. ATLAS has an excellent hermeticity and is able to cover pseudorapidity regions up to $|\eta| = 4.9$. Typically, physics analysis consider objects in the pseudorapidity region $|\eta| < 2.5$. For a quick visualization of the correspondence in terms of polar angle distribution, some pseudorapidity values are reported in Table 2.2.

θ	0°	5°	10°	20°	30°	45°	60°	80°	90°
η	∞	3.13	2.44	1.74	1.31	0.88	0.55	0.175	0

Table 2.2: Pseudorapidity vs polar angle values.

2.1.2 Magnets

ATLAS is provided with four superconducting magnets that allow the measurement of charged particles momenta by curving their trajectory.

A central solenoid sits around the inner detector and produces a 2 T magnetic field along the direction parallel to the beam axis. It is only 45 mm thick (equivalent to 0.66 radiation lengths X_0) and is cooled with liquid Helium, sharing the cryostat with the electromagnetic calorimeter.

Paired to the muon spectrometer, the superconducting air-core toroid magnet (Figure 2.5) has an open structure with eight superconducting toroidal coils in the barrel part and two end-cap systems made of eight coils. The field strength varies strongly with ϕ : in the barrel region ($|\eta| < 1.4$) is 1.5-5.5 Tesla·m; in the end-caps ($1.6 < |\eta| < 2.7$) 1-7.5 Tesla·m. Such configuration of the magnets gives a field orthogonal to the muons trajectory.

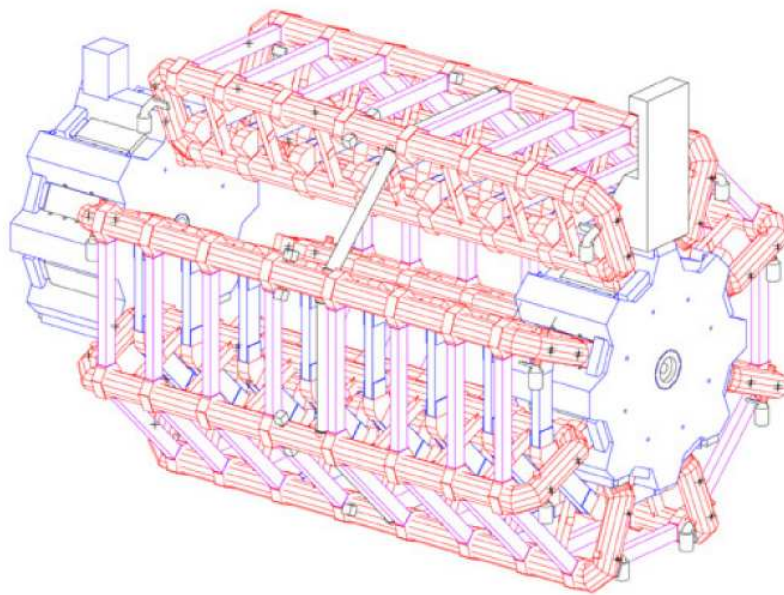


Figure 2.5: Toroidal magnet system.

2.1.3 Inner detector

The Inner Detector (ID) is the subsystem closest to the IP and tracking charged particles arising from collisions allows for the measurement of their momentum and vertex reconstruction with excellent resolution. At the design choices level, radiation resistance had to be taken into account, as well as reducing the amount of material to be placed in front of the calorimeters to avoid spoiling the energy measurement. This quantity varies between 0.5 and 2.5 X_0 depending on the pseudorapidity region, most of it coming from supporting equipment. This material is responsible for photon conversions and electron bremsstrahlung.

The ID is surrounded by the central solenoid magnet (Section 2.1.2) and is composed by three subsystems, from the closest to the furthest from the IP: a pixel detector, a silicon

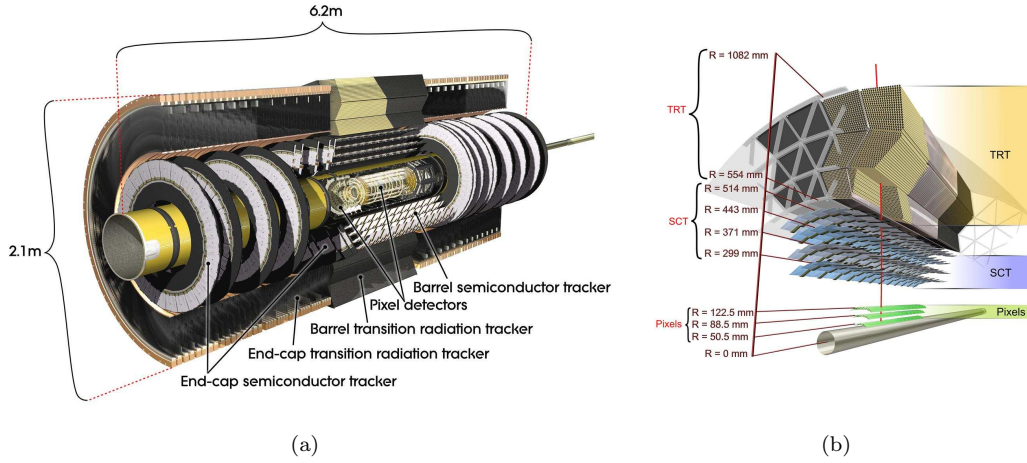


Figure 2.6: (a) Schematic of the ID system. (b) Detailed schematic of the barrel section of the ID showing the three subsystems and reporting the distance to the center of the beam pipe.

strip detector and a straw detector (Figures 2.6(a) and 2.6(b)).

Silicon Detectors

The first subsystem covers the region $|\eta| < 2.5$ and is composed by three cylindrical layers in the barrel region, each of them distant from the beam by 50.5 mm, 88.5 mm and 122.5 mm respectively, and by three concentric discs in the end-cap region, each of them distant from the beam by 49.5 mm, 58.0 mm and 65.0 mm respectively. Each silicon pixel has a size of $50 \times 400 \mu\text{m}^2$ and is $250 \mu\text{m}$ thick, with in total ~ 80.4 million readout channels to achieve a very fine granularity. The precision is of $10 \mu\text{m}$ in $R\phi$ and $115 \mu\text{m}$ in Z and R in the barrel and end-cap region respectively.

The very first layer is called B -layer as, thanks to its position really close to the IP, allows for the reconstruction of secondary vertices associated with the production of short lived particles such as B -hadrons. This information is very useful to identify particle jets from b quarks⁴.

After the three layers of pixel detectors, come four layers of silicon strip detectors. The SemiConductor Tracker (SCT) also covers the region $|\eta| < 2.5$ with a barrel and end-cap design similar to the pixel detector one, being composed by eight silicon bands (two per layer) 128 mm long and $80 \mu\text{m}$ large. It makes use of ~ 6.3 millions readout channels and the resolution achieved is of $17 \mu\text{m}$ in $R\phi$ and $580 \mu\text{m}$ in Z and R in the barrel and end-cap region respectively.

By allowing for four redundant position measurements⁵, the SCT contributes mainly to the momentum reconstruction.

⁴The b -tagging technique will be discussed in

⁵One of the coupled layers is rotated of 40mrad with respect to the other, which is parallel to the axis, giving a small stereo angle for a redundancy in the ϕ coordinate measurement.

Transition Radiation Tracker

In order to reduce the amount of material in front of the calorimeters, and to reduce the construction costs as well, in the third subsystem the semiconductor technology has been substituted with straw detectors. The Transition Radiation Tracker (TRT) consists of thin proportional chambers made of straw polyimide drift tubes, 4 mm in diameter. The drift tubes are filled with a gas mixture composed of: 70% Xenon, 27% Carbon Dioxide, 3% Oxygen. The anode collecting the electrons from the ionized gas at the passage of the charged particle is made of tungsten covered in gold.

In the barrel region the tubes are 144 cm long and placed parallel to the beam axis, while in the end-cap region they are 37 cm long and positioned radially in wheels, with layers of radiator foils alternated to layers of straws. The resolution achieved is of $130 \mu\text{m}$ in $R\phi$ and $Z\phi$ in the two regions respectively. The covered pseudorapidity region is of $|\eta| < 2.0$ and the readout is composed by ~ 351000 channels.

About 36 measurements per track are taken, and since each channel provides two independent thresholds per hit, it is possible to discriminate between electrons and pions, since the firsts will more probably reach the high threshold.

In the end, the combination of the three ID subsystems gives very precise $R\phi$ and Z measurements, as well as good track pattern recognition. The resolution on the transverse momentum, measured with cosmic muon calibration runs [10], is:

$$\frac{\sigma_{p_T}}{p_T} = P_1 \oplus P_2 \times p_T, \quad (2.7)$$

where $P_1 = 1.6 \pm 0.1\%$ and $P_2 = (53 \pm 2) \times 10^{-5} \text{ GeV}^{-1}$. This means a resolution of $\sim 1.6\%$ for tracks with $p_T \sim 1 \text{ GeV}$ and $\sim 50\%$ for tracks with $p_T \sim 1 \text{ TeV}$.

2.1.4 Calorimeters

Particles leaving the ID and surviving the crossing of the central solenoid magnet will face the calorimeter system, depicted in Figure 2.7. The full system is characterized by a coverage in pseudorapidity up to $|\eta| < 5$ and an almost full coverage in ϕ . With its $22 X_0$ and $24 X_0$ of material in the barrel and end-cap regions respectively it is also able to stop most of the non-muon particles from the interaction. Besides particles energy measurement, the calorimeters provide particle identification information, discriminating electrons, photons and jets, and the determination of the missing transverse energy.

Different technologies are used in the barrel, end-cap and forward regions for both the electromagnetic and the hadronic calorimeters. All of them are sampling calorimeters, with a dense medium acting as absorber to stop particles and start showers, and an active material to detect the signal from ionization. For the electromagnetic calorimeters and the forward hadronic calorimeter liquid argon is used as active medium, while the barrel and extended-barrel hadronic calorimeter uses scintillating tiles. The liquid argon is cooled at a temperature of about 88 K, with the use of two sets of cryostats: the barrel electromagnetic calorimeter shares the cryostat with the central solenoid; the end-cap and forward electromagnetic calorimeter and the hadronic end-cap calorimeter share a cryostat in the forward region.

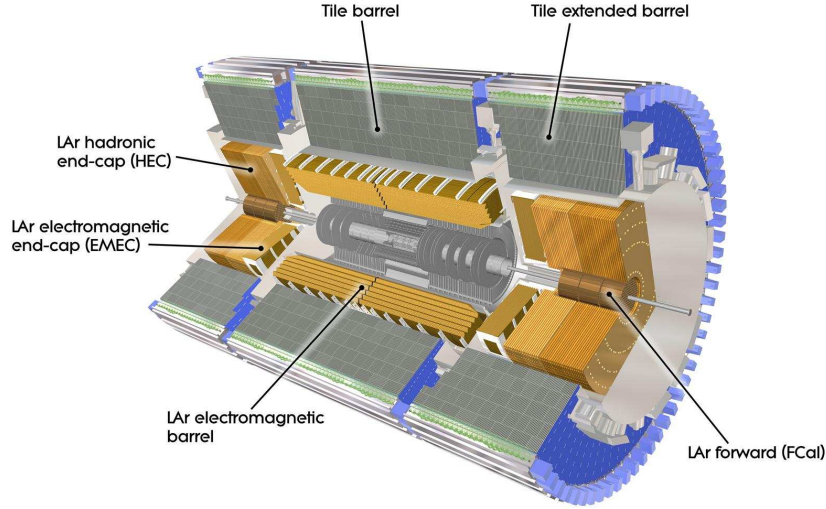


Figure 2.7: Schematic of the calorimeter complex of the ATLAS detector.

265 The processes involved in the shower formation are bremsstrahlung $e^\pm \rightarrow e^\pm + \gamma$ and
 266 pair production $\gamma \rightarrow e^+e^-$. For particles with energies lower than about 100MeV ionization
 267 processes are dominating. In general, these cascade of events continues until a certain
 268 threshold is reached, and the final number of particles produced is proportional to the
 269 energy of the first particle originating the shower.

The performance for the energy resolution is parametrized by the following formula:

$$\frac{\sigma_E}{E} = \frac{a}{\sqrt{E}} \oplus \frac{b}{E} \oplus c, \quad (2.8)$$

270 where the terms of the sum correspond, respectively, to a statistical term related to how
 271 shower develops in the sampling calorimeter; to an instrumental term including readout elec-
 272 tronic rumor effects; to a systematic term that depends on calibration, shower containment,
 273 inactive material and on the linearity of the response as well.

The energy resolution measured in test-beam runs for the liquid argon calorimeters is [11]:

$$\frac{\sigma_E}{E} = \frac{10\%}{\sqrt{E}} \oplus \frac{170 \text{ MeV}}{E} \oplus 0.7\%, \quad (2.9)$$

while for the hadronic barrel calorimeter is [12]:

$$\frac{\sigma_E}{E} = \frac{50\%}{\sqrt{E}} \oplus 3\%. \quad (2.10)$$

274 Electromagnetic calorimeter

275 The electromagnetic calorimeter, also called LAr calorimeter (from Liquid Argon), can
 276 measure electrons and photons energies in the range from 50 MeV and 3TeV. In the barrel

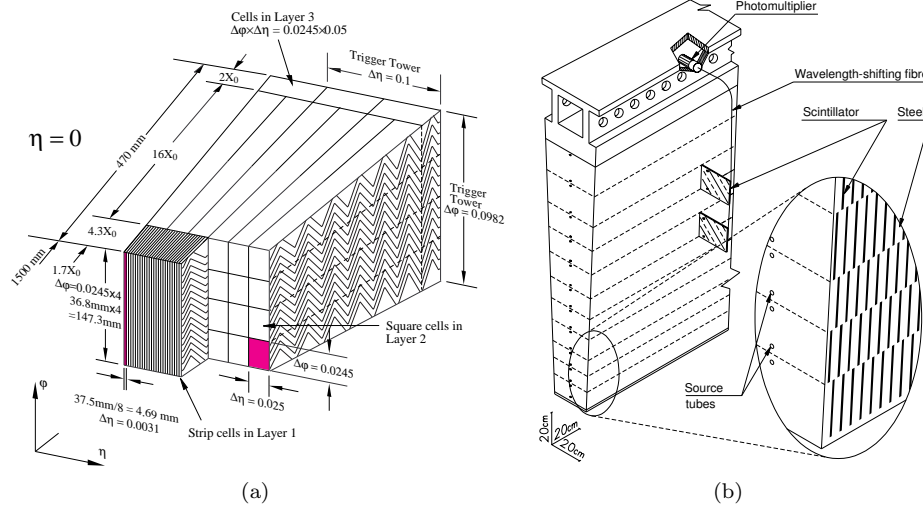


Figure 2.8: (a) Schematic drawing of a module of the Electromagnetic barrel calorimeter. (b) Schematic drawing of a module of the Hadronic barrel calorimeter.

region it is referred to as EMB (ElectroMagnetic Barrel), is divided into two identical semi-barrels EMBA and EMBC separated at $Z=0$ by a 6 mm gap and covers the pseudorapidity region $|\eta| < 1.475$. Two end-cap detectors (EMEC, ElectroMagnetic End-Cap), divided into two coaxial wheels, cover the pseudorapidity regions $1.375 < |\eta| < 3.2$. A pre-sampler, extended over $|\eta| < 1.8$, stands in front of the EMB and allows for the measurement of the energy the particles lost before reaching the EMB i.e. crossing the material of the ID, the central solenoid and the cryostat.

The absorbing material is lead shaped into an accordion geometry to achieve full symmetry in ϕ , as shown in the drawing of Figure 2.8(a). Signal from the ionization produced in the liquid argon is collected by an electrode in the middle of the active material region, fixed into a honeycomb structure.

Three longitudinal regions in the EMB are designed for different tasks. The first sample, $4.3X_0$ long, is finely segmented in η to precisely measure the direction in pseudorapidity of the particles with thin readout strips of $\Delta\eta \times \Delta\phi = 0.0031 \times 0.098$. This helps for photon/ π^0 discrimination and as well for separate close-by γ s from π^0 decay.

The second piece, $16X_0$ long, contains the bulk of electrons and photons energy deposit. It is divided in towers with dimension $\Delta\eta \times \Delta\phi = 0.025 \times 0.0245$ and provides the position measurement of the cluster. The 95% of the energy of the shower is deposited in a matrix of 3×7 towers $\Delta\eta \times \Delta\phi$.

The third layer, $2X_0$ long, is coarsely segmentes and collects the last bit of the longitudinal development of the electromagnetic showers. Towers in this region have a dimension of $\Delta\eta \times \Delta\phi = 0.05 \times 0.0245$.

Also the EMEC is divided in three longitudinal samples (two in the region $1.375 < |\eta| < 1.5$), and besides the lead, also the thickness of the liquid argon layers are varied in the radial direction.

The thickness of the absorber layers depend on the pseudorapidity in order to make par-

tiles entering the system with different incident angles cross the same amount of material.

Hadronic end-cap calorimeter

The Hadronic End-Cap calorimeters (HEC) use copper as passive material and liquid argon as active material, chosen for its radiation hardness in a region ($1.5 < |\eta| < 3.2$) exposed to a significant amount of particle flux. Each HEC is composed by two independent wheels with granularity varying with η : in $1.5 < |\eta| < 2.5$ $\Delta\eta \times \Delta\phi$ is 0.1×0.1 in the first two longitudinal layers, 0.2×0.1 in the last one; in $2.5 < |\eta| < 3.2$ $1.5 < |\eta| < 2.5$ $\Delta\eta \times \Delta\phi = 0.2 \times 0.2$ in all the three samples.

The HECs collect the energy from particles that are not completely contained in the EMECs and in particular are used to reconstruct jets and the missing transverse energy.

Forward calorimeter

The Forward Calorimeter (FCal) cover the very forward region of pseudorapidity $3.1 < |\eta| < 4.9$ making the calorimeter system achieve its good hermeticity and minimize the energy losses. It has an electromagnetic part that uses copper as absorber and two hadronic compartments with tungsten as passive material.

Hadronic barrel calorimeter

The hadronic calorimeter in the barrel and extended barrel region, going up to $|\eta| < 1.7$, is made of scintillating tiles as active material with lead as absorber and is commonly referred to with the name of TileCal. The light in the ultraviolet range that is generated in the tiles is collected through wavelength shifting optical fibres. As can be seen in the drawing of Figure 2.8(b), the tiles are slightly rotated, to allow showers cross them from the side.

TileCal sits just after the electromagnetic calorimeter and measures the energy and position of jets and isolated hadrons. It is divided in depth in three layers with varying length (1.4, 4.1, 1.8 hadronic interaction lengths λ in the barrel and 1.5, 2.6, 3.3 λ in the extended barrel) and segmentation ($\Delta\eta \times \Delta\phi = 0.1 \times 0.1$ in the first two layers, $\Delta\eta \times \Delta\phi = 0.2 \times 0.1$ in the third), and in 64 slices in ϕ , each of $\Delta\phi \sim 0.1$.

The readout channels are grouped into cells that form a pseudo-projective geometry in η .

2.1.5 Muon spectrometer

The most external detector system is the muon spectrometer, a combination of toroidal superconducting magnets (Section 2.1.2) and precision chambers providing a measurement of the momentum of muons in $|\eta| < 2.7$ in addition to the measurement from the ID. It is also equipped with an independent trigger system used for the first event triggering stage (see Section 2.1.6) active in the pseudorapidity region $|\eta| < 2.4$.

Four sub-detectors compose the muon system: Monitored Drift-Tube (MDT) chambers, Cathode Strips Chambers (CSC), Resistive Plate Chambers (RPC) and Thin Gap Chambers (TGC). The layout changes in the barrel and end-cap regions, and is schematically shown in Figure 2.9(b): in the barrel region, chambers are arranged in three cylindrical layers around

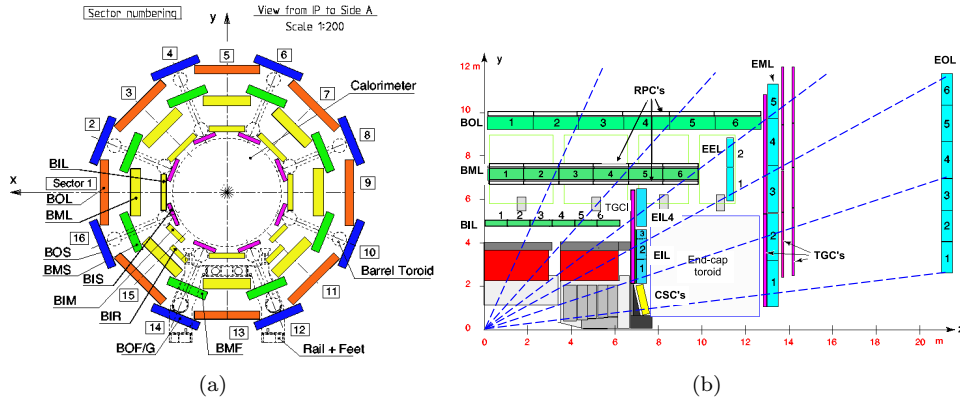


Figure 2.9: (a) Cross section of the barrel muon system. (b) Lateral section of the muon system. Barrel MDTs are shown in green, end-caps MDTs in light blue, CSC in yellow, TGCs in magenta, RPCs in white.

the beam axis, one layer being inside the magnet; in the end-caps these three layers are placed perpendicular to the beam axis.

Detection chambers

MDTs and CSCs are used to detect muons in the pseudorapidity regions $|\eta| < 2.0$ and $2.0 < |\eta| < 2.7$ respectively. MDTs are proportional chambers constituted by aluminium pressurised drift tubes with a diameter of 30 mm and length varying from 0.9 m to 6.2 m. The gas mixture in them is 93% argon and 7% carbon dioxide, the anode is a 50 μm tungsten-rhenium wire producing a radial electric field. Each chamber is composed by a group of six or eight tubes placed transverse to the beam axis. This number of tubes allows for a very good track reconstruction and high reduction of the fake tracks from random associations of background hits, providing a resolution on position of 80 μm .

The CSCs are used at higher η to better deal with the higher particle flux. They are arranged in a system of two disks with eight chambers each. Each chamber contains four multiwire proportional chambers (the CSCs) with wires oriented in the radial direction, spaced by 2.5 mm and in the same gas mixture of argon and carbon dioxide as the MDTs. The cathode strips are oriented one perpendicularly to the anode wires (and gives the precision coordinate) and the other parallelly to the wires (and gives the transverse coordinate). The resolution provided by the interpolation between the charges induced on neighbouring cathode strips ranges between 50 and 70 μm .

Trigger chamber

For trigger purposes detectors quicker than drift tubes are needed⁶. MDTs and CSCs are then coupled with special layers of trigger chambers: in the barrel region, the MDT's second layer is covered on both sides by RPCs, while MDT's third layer is covered by a

⁶Drift-time in tubes with a diameter of $\mathcal{O} \sim 10$ mm can be of ~ 500 ns, too long with respect to the 25 ns spacing of the bunch crossings.

RPC alternatively on the inner and outer side; in the endcaps, TGCs cover the inner side of MDT's first and third layers.

A RPC is a detector with a gas-gap between two resistive bakelite plates separated by 2 mm and containing a gas mixture of $\text{C}_2\text{H}_2\text{F}_4$ (94.7%), $\text{Iso-C}_4\text{H}_{10}$ (5%) and SF_6 (0.3%). RPCs measure six points per coordinate for each particle, quickly collecting the avalanches with two orthogonal sets of pick-up strips that provides a position resolution of 1 cm in each plane and 1 ns time resolution, allowing for individual bunch crossing discrimination. Also RPCs provide the ϕ coordinate for the tracks in the final analysis, since MDTs only give the η coordinate.

TGCs are similar to CSCs, have 1.8 mm wire-to-wire separation and 1.4 mm wire-to-cathode separation. They use a highly quenching gas mixture of CO_2 55% and $\text{n-C}_5\text{H}_{12}$ 45% and provide a spatial resolution of about 1 mm and a time resolution of 5 ns.

2.1.6 Trigger system

It was already introduced at the beginning of this Chapter the issue faced by LHC experiments of dealing with a huge amounts of events at very high frequencies. We remind that considering the nominal LHC luminosity of $10^{34} \text{ cm}^{-2} \text{ s}^{-1}$ a rate of interactions of 1 GHz is expected! This poses serious technical difficulties as the maximum frequency at which data can be recorded is limited to 200 Hz considering the limited capacity for storage.

ATLAS developed a trigger system able to reduce by a factor of 10^6 the amount of data to be kept by selecting only interesting physics events. The system is divided in three levels characterized by increasing sophistication and diminishing speed. At the very first indeed we will need a really quick and simple criterium to reject useless events. The reduced information can then be processed with somehow slower logic by the other two High Level Triggers (HLT). A drawing of the system is shown in Figure 2.10.

Most of the trigger chains used for physics are un-scaled in the sense that all the events passing the selection are kept, but there are also pre-scaled trigger chains that contain either too many events or events considered not physically interesting. These trigger chains are used for checks or calibration rather than physics analysis.

Level 1 trigger

The Level 1 trigger (L1) is completely based on the hardware of the detector, taking information from calorimeters and from the muon spectrometer trigger systems RPC and TGC (Section 2.1.5) at 40 MHz (the frequency of the beam crossing) and reducing it to 75 kHz by choosing events with high transverse momentum or high missing transverse energy.

Using dedicated fast front-end electronics (the typical decision time being less than $2 \mu\text{s}$), calorimeter cells are analogically summed to build calorimetric towers which, if having an energy higher than a certain threshold, will activate a trigger chain.

These trigger chains will then be combined with the information from the muon spectrometer to form the so-called Region of Interest (RoI) that is passed to the next trigger level.

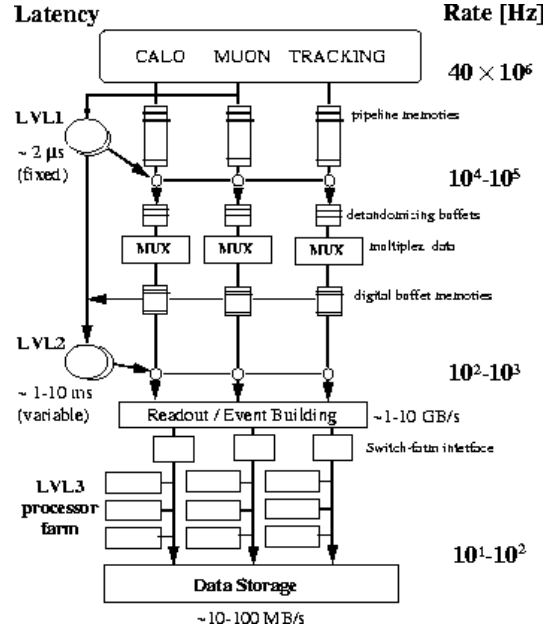


Figure 2.10: Schematic drawing of the three-level trigger system of ATLAS.

Level 2 trigger

Starting from the RoI, the Level 2 trigger (L2) will reduce the 75 kHz to 3.5 kHz of events with an average decision time of 40 ms. At this stage the information from the trackers is incorporated to the RoI to build candidate object (electrons, photons, muons) and better obtain its position and energy with simplified algorithms quick enough to respect the limit on the decision time.

Level 3 trigger

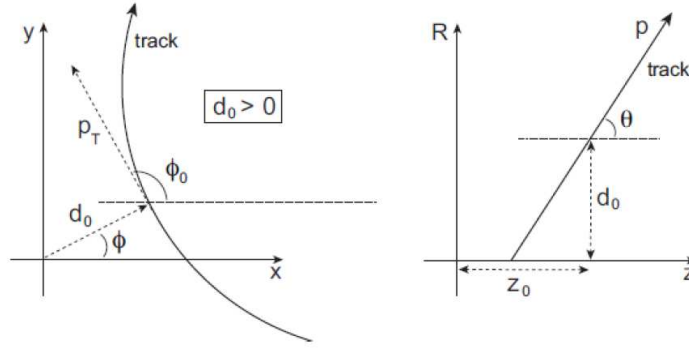
The last trigger, Level 3, is called Event Filter (EF) since at this point the physics objects are built using the same algorithms as the off-line reconstruction. With an execution time amounting to 4 s, the EF reduces the event rate to the goal value of 200 Hz.

2.2 Object reconstruction

After having described the ATLAS detector, in the following Section we will explain how object (electrons, muons, jets and the missing transverse energy E_T^{miss}) are reconstructed to be used in physics analyses [13]. Details from selections specific for the analyses presented in this dissertation are given.

2.2.1 Electrons

Electrons [14] are reconstructed for pseudorapidities up to $|\eta| = 2.5$, where information from the ID is available, matching a track with an energy deposit (cluster) in the electro-



(a)

Figure 2.11: Schematic drawings of the parameters used for track reconstruction in the XY and RZ planes (left and right respectively) where the origin is the reconstructed primary vertex⁷. The parameters are: q/p , the charge divided by the momentum; θ , or more used η , the angle with respect to the Z axis in the RZ plane measured from the perigee; ϕ_0 , the angle with respect to the X axis in the XY plane measured from the perigee; d_0 , the impact parameter, or perigee with respect to the Z axis in the XY plane; z_0 , Z component of the perigee.

420 magnetic calorimeter.

421 To identify tracks from ID points an inside-out algorithm is used, starting from a seed
 422 of three aligned hits in the pixel detector or in the SCT. Five fundamental parameters,
 423 shown and described in Figure 2.11, are computed and used for the subsequent steps of
 424 hits association. The candidate track must be formed by at least seven points measured in
 425 the silicon detectors, d_0 must be lower than 10 mm and the transverse momentum must be
 426 higher than 150 MeV.

427 Clusters [15] are built starting from $\Delta\eta \times \Delta\phi = 0.025 \times 0.025$ single energy deposits
 428 summing up into towers. Adjacent towers form clusters of 3×7 cells units in $\eta \times \phi$ in
 429 $|\eta| < 1.4$ and 5×5 further. Of all the candidate reconstructed tracks, those extrapolated to
 430 the calorimeter with the smallest ΔR with respect to the energy cluster is chosen.

431 For our analyses, electrons in the transition region $1.37 < |\eta_{\text{cluster}}| < 1.52$ with inactive
 432 material are excluded. Electrons are also required to have $E_T = E_{\text{cluster}} / \cosh \eta_{\text{track}} >$
 433 25 GeV and $z_0 < 2$ mm. They have to be separated from any jet (Section 2.2.3) selected by
 434 at least $\Delta R = 0.4$. 90% efficient isolation cuts to reduce the background from non-prompt
 435 electrons coming from hadron decays are defined, one based on the energy from calorimeter
 436 cells surrounding the candidate in a cone of radius $R = 0.2$ and the other based on the track
 437 transverse momenta sum in a cone of radius $R = 0.3$ around the electron.

438 2.2.2 Muons

439 Track segments reconstructed in the muon spectrometer are matched to tracks from the
 440 ID to build muon candidates. The combined tracking information has to give $p_T > 25$ GeV

⁷Of the reconstructed vertexes consistently in the beam collision region in the XY plane with at least five associated tracks, the one with the highest number of tracks is taken as the primary one.

and $|\eta| < 2.5$, and z_0 has to be lower than 2 mm. The muon radial distance from any selected jet is required to be $\Delta R > 0.4$.

A p_T -dependent track-based isolation condition is defined as follows: the scalar p_T sum of all tracks (except for the muon track itself) in a cone of variable radius $R = 10 \text{ GeV}/p_T^\mu$ around the lepton must be less than 5% of the muon p_T . This isolation requirement works well also in high pile-up events or in the case the muon is close to a jet.

2.2.3 Jets

Jets from quark hadronization are reconstructed using the anti- k_t algorithm [16, 17, 18] with a radius parameter $R = 0.4$ (from which the algorithm is often referred to as anti- k_t4) using calorimeter energy deposits⁸ corrected for effects of non-compensation, dead detector material and out-of-cluster leakage using local cluster calibrations [19, 20].

To subtract contributions from in-time and out-of-time pile-up interactions a correction is applied parameterized according to the number of primary vertices in the event and the number of average interactions in the luminosity block ($\langle \mu \rangle$) as a function of jet pseudorapidity. Jets are finally calibrated to the hadronic scale using p_T - and η -dependent correction factors derived from Monte Carlo simulation [21]. For the analyses that we will present, only jets with $p_T > 25 \text{ GeV}$ and $|\eta| < 2.5$ are considered.

A variable called “jet vertex fraction” (JVF) is defined as the fraction of the sum of p_T of tracks with $p_T > 1 \text{ GeV}$ associated with the jet that comes from tracks originating from the primary vertex. By requiring $\text{JVF} > 0.5$ we avoid selecting jets from in-time pile-up events.

Since energy deposits from electrons can be reconstructed as jets, if jets are found within ΔR of 0.2 of a selected electron, the jet closest to the lepton is discarded in order to avoid double-counting of electrons as jets. After this one jet has been removed, electrons that lie within $\Delta R < 0.4$ of the jets remaining are removed.

A technique to identify jets from the hadronisation of bottom quarks, called b -tagging [22], is used. It makes use of multivariate techniques combining the information from secondary and tertiary decay vertices found within the jet and from the impact parameters of displaced tracks to obtain a b -tagging weight that discriminates between b and not- b jets. A working point for this weight is chosen by finding a compromise between a good efficiency (the ratio between tagged b -jets and true b -jets) and a high light-jet rejection (the inverse of the number of light-jets misidentified as b -jets). For our analyses, a working point corresponding to 70% efficiency, ~ 130 light-jet rejection and a charm-jet rejection of 5 is chosen⁹.

2.2.4 Missing transverse energy

To estimate the momentum of invisible particles in the event, the missing transverse energy E_T^{miss} [23] is defined by first matching each calorimeter energy deposit with a high- p_T lepton or jet. After the energies of these objects are corrected accordingly to the respective calibration constants, the calorimeter clusters that did not get associated with any high- p_T object are calibrated for energy losses in dead material regions and for the different response

⁸Topological clusters, abbreviated as “topo-clusters”, are built from neighboring calorimeter cells starting from a seed deposit with a signal to noise ratio higher than a certain threshold. Topo-clusters are treated as massless and their energy at the electromagnetic scale is the sum of the constituent cells.

⁹These values refer to jets with $p_T > 20 \text{ GeV}$ and $|\eta| < 2.5$ in simulated $t\bar{t}$ events.

479 to the electromagnetic and hadronic components of particle showers. Finally the $E_{\text{T}}^{\text{miss}}$ is
480 computed from the combination of the vector sum of the calibrated cluster momenta and a
481 term associated with muon momenta.

483 Monte Carlo simulation

484

485 **3.1 Parton shower**

486 **3.2 Hadronization**

487 **3.3 Underlying-event**

488 **3.4 Generators**

490 Searches for vector-like top partner 491 pairs in the single lepton channel

492

493

494 In the following Chapter we will describe two searches for vector-like top partners $T\bar{T}$
 495 pairs performed in the single lepton channel. These analyses are optimized for different final
 496 states and are thus complementary. The first search focuses on decay channels with high BR
 497 to Wb and is performed using the full dataset of p-p collisions at the center of mass energy
 498 of $\sqrt{s}=8$ TeV collected during 2012 at the ATLAS detector, consisting in 20.34 fb^{-1} , while
 499 the preliminary search for vector-like top partners with high BR to Ht uses a partial dataset
 500 of the same data, amounting to 14.3 fb^{-1} .

501 The Chapter is organized as follows: Section 4.2.1 and Section 4.2.2 present respectively
 502 the data and Monte Carlo samples used in the searches, which are in general common to
 503 both analyses with only few exceptions that are reported; Section 4.2.3 describes how the
 504 multi-jet background from QCD events is obtained; Section ?? contains a brief reminder of
 505 object definition. Finally, the two analyses are detailed in Section 4.3 and Section 4.4, which
 506 illustrate the event selection criteria, the background modeling estimation, the systematics
 507 affecting the analysis, the statistical treatment and the results.

508 **4.1 Common event preselection and orthogonality**

509 **4.2 Datasets**

510 **4.2.1 Data sample**

511 **4.2.2 Monte Carlo simulated samples**

512 **SM processes**

513 **Signal samples**

514 **4.2.3 Multi-jet background**

515 **4.3 Search for $T\bar{T}$ pairs decaying to $Wb + X$**

516 **4.3.1 Boosted W reconstruction**

517 **4.3.2 Control regions**

518 **4.3.3 Event selection**

519 **4.3.4**

520 **4.3.5**

521 **4.3.6 Systematics**

522 **4.4 Preliminary search for $T\bar{T}$ pairs decaying to $Ht + X$**

523 **4.4.1 Control regions**

524 **4.4.2 Event selection**

525 **4.4.3**

526 **4.4.4**

527 **4.4.5 Systematics**

529 Statistical treatment and Results

530

531 5.1 The CL_s method

532 5.2 Results

533 Conclusions

534

540 **Search for $T\bar{T} \rightarrow Wb + X$ at $\sqrt{7}$ TeV**

541

Bibliography

- [1] J. Aguilar-Saavedra, *Identifying top partners at LHC*, **JHEP** **0911** (2009) 030, [arXiv:0907.3155 \[hep-ph\]](#).
- [2] S. P. Martin, *Extra vector-like matter and the lightest Higgs scalar boson mass in low-energy supersymmetry*, **Phys.Rev.** **D81** (2010) 035004, [arXiv:0910.2732 \[hep-ph\]](#).
- [3] ATLAS Collaboration, *The ATLAS Experiment at the CERN Large Hadron Collider*, **JINST** **3** (2008) S08003.
- [4] L. Evans, P. Bryant (Eds.), *LHC Machine*, **JINST** **3** (2008) S08001.
- [5] CMS Collaboration, *The CMS experiment at the CERN LHC*, **JINST** **3** (2008) S08004.
- [6] ALICE Collaboration, *The ALICE experiment at the CERN LHC*, **JINST** **3** (2008) S08002.
- [7] LHCb Collaboration, *The LCHb experiment at the CERN LHC*, **JINST** **3** (2008) S08005.
- [8] M. Lamont, *The First Years of LHC Operation for Luminosity Production*, in *Proceedings of 4th International Particle Accelerator Conference (IPAC 2013)* (2013) .
- [9] ATLAS Collaboration. <https://twiki.cern.ch/twiki/bin/view/AtlasPublic/LuminosityPublicResults>.
- [10] ATLAS Collaboration, *Studies of the performance of the ATLAS detector using cosmic-ray muons*, **Eur. Phys. J.** **C** **71** (2011) 1593.
- [11] ATLAS Collaboration, *Readiness of the ATLAS liquid argon calorimeter for LHC collisions*, **Eur. Phys. J.** **C** **70** (2010) 723–753.
- [12] ATLAS Collaboration, *Readiness of the ATLAS Tile calorimeter for LHC collisions*, **Eur. Phys. J.** **C** **70** (2010) 11931236.

- [13] ATLAS Collaboration, *Expected Performance of the ATLAS Experiment - Detector, Trigger and Physics*, [arXiv:0901.0512 \[hep-ex\]](#).
- [14] ATLAS Collaboration, *Electron performance measurements with the ATLAS detector using the 2010 LHC proton-proton collision data*, *Eur. Phys. J. C* **72** (2012) no. 3, 1909.
- [15] W. Lampl et al., *Calorimeter clustering algorithms: Description and performance*, ATL-LARG-PUB-2008-002 (2012) . <https://cdsweb.cern.ch/record/1099735>.
- [16] M. Cacciari, G. P. Salam, and G. Soyez, *The anti- k_t jet clustering algorithm*, *JHEP* **04** (2008) 063, [arXiv:0802.1189v2 \[hep-ph\]](#).
- [17] M. Cacciari and G. P. Salam, *Dispelling the N^3 myth for the k_t jet-finder*, *Phys. Lett. B* **641** (2006) 57, [arXiv:0512210v2 \[hep-ph\]](#).
- [18] M. Cacciari, G. P. Salam, and G. Soyez, *FastJet User Manual*, *Eur. Phys. J. C* **72** (2012) 1896, [arXiv:1111.6097 \[hep-ph\]](#).
- [19] C. Cojocaru et al., *Hadronic calibration of the ATLAS liquid argon end-cap calorimeter in the pseudorapidity region $1.6 < |\eta| < 1.8$ in beam tests*, *Nucl. Instr. Meth. A* **531** (2004) 481, [arXiv:0407009 \[physics\]](#).
- [20] T. Barillari et al., *Local hadronic calibration*, ATL-LARG-PUB-2009-001 (2009) . <https://cds.cern.ch/record/1112035>.
- [21] ATLAS Collaboration, *Jet energy measurement with the ATLAS detector in proton-proton collisions at $\sqrt{s} = 7$ TeV*, *Eur. Phys. J. C* **73** (2013) 2304, [arXiv:1112.6426 \[hep-ex\]](#).
- [22] ATLAS Collaboration, *Commissioning of the ATLAS high-performance b -tagging algorithms in the 7 TeV collision data*, ATLAS-CONF-2011-102 (2011) . <https://cds.cern.ch/record/1369219>.
- [23] ATLAS Collaboration, *Performance of Missing Transverse Momentum Reconstruction in Proton-Proton Collisions at 7 TeV with ATLAS*, *Eur. Phys. J. C* **72** (2012) 1844, [arXiv:1108.5602 \[hep-ex\]](#).